Supplementary Information

Mutations in *DONSON* disrupt replication fork stability and cause microcephalic dwarfism.

Supplementary Table 1: Clinical phenotype data of individuals with DONSON mutations

Clinical information relating to individuals with *DONSON* mutations. Wgt, weight (kg); Hgt, height (cm); Lgth, length (cm); SD, standard deviation from the population mean for age and sex; OFC, occipital frontal circumference; GORD, gastro-oesophageal reflux disease; ID, intellectual disability; ADHD, attention deficit hyperactivity disorder; FA, Fanconi anaemia. [a]measurement taken at 5 weeks of age. [b]measurement taken at 4 months of age. [c]measurement taken at 2 weeks of age. [d]term gestation assumed for SD calculation. [e]fetal death. [f]antenatal USS scan. [g]at 19 wk scan, standard deviation calculated using Fenton growth chart[61].

Supplementary References:

61. Fenton, T.R. & Kim, J.H. A systematic review and meta-analysis to revise the Fenton growth chart for preterm infants. *BMC Pediatr* **13**, 59 (2013).

Supplementary Table 2. Common ancestral haplotype (blue) flanking the DONSON locus in families P1, P2, P3 and P6.

SNP	position[b]	gene	coding	Ref	Alt	P1-1	P1-2	P2	P3	P6	MAF[c]
rs121913215	34804930	*IFNGR2*	intronic	A	T	AT	AT	AT	AT	AA	0.0010
rs75398504	34839530	*TMEM50B*	intronic	G	A	GA	GA	GA	GA	GG	0.0006
rs144266803	34861444	*DNAJC28*	T86I	G	A	GA	GA	GA	GA	GA	0.0010
rs148155071	34876289	*GART*	3'UTR	A	T	AT	AT	AT	AT	AT	0.0026
rs151206034	34889888	*GART*	M577T	A	G	AG	AG	AG	AG	AG	0.0010
rs139633075	34897281	*GART*	L365V	G	C	GC	GC	GC	GC	GC	0.0010
rs187476997	34902228	*GART*	intronic	T	C	TC	TC	TC	TC	TC	0.0016
rs142038738	34903861	*GART*	E177D	C	A	CA	CA	CA	CA	CA	0.0009
rs148794591	34924549	*SON*	A1004A	T	C	TC	TC	TC	TC	TC	0.0010
rs142751481	34925936	*SON*	I1467V	A	G	AG	AG	AG	AG	AG	0.0010
rs146664036	34951753	***DONSON***	**K489T**	T	G	TG	TG	TG	TG	TG	0.0010
rs192585552	34956005	***DONSON***	**c.786-33**	T	C	TC	TC	TC	TC	TC	0.0005
no rsID[a]	34960866	***DONSON***	**S28R**	T	G	TG	TG	TG	TG	TG	-
rs190141427	34967690	*CRYZL1*	3'UTR	T	G	TG	TG	TG	TG	TG	0.0006
rs184229251	34989145	*CRYZL1*	intronic	T	C	TC	TC	TC	TC	TC	0.0006
rs570210988	36261887	*RUNX1*	intronic	C	C	CC	CC	CT	CC	CC	0.0002

Analysis of rare variants identified through exome sequencing demonstrated a common ancestral haplotype extending 127.7 kb in DONSON patients heterozygous for the 'haplotype' disease allele. Parents of P2 and P3 were also exome sequenced, allowing phasing of alleles across this haplotype. No other variants were identified in trans in the genes within this region in any individuals apart from DONSON – the in trans variants in DONSON are omitted here for clarity. [a]This variant lies within a GC rich region and therefore is not covered in many control population datasets. [b]Genomic position using hg19 coordinates. [c]Minor allele frequencies taken from ExAC or 1000 Genomes data.

Supplementary Table 3 – Proteomic mass spectrometry screen for GFP-DONSON interactors.

DONSON proteomics screen (related to **Fig. 4a**). Cell extracts of GFP or GFP-DONSON HeLa Flp-In/T-Rex cells were prepared (-Tet; uninduced cells: Asynch; asynchronously growing cells: S-phase; cells treated with 2 mM HU to arrest cells in S-phase). GFP or GFP-DONSON was isolated and digested on-beads. Peptides were identified by mass spectrometry and quantified by LFQ by the MaxQuant software package with a 1% FDR. Contaminants and reverse data base hits were deleted. Sheet 1: GFP-DONSON protein interactors. Proteins enriched by GFP-DONSON were identified by Student t-test and ratio cut-off against the respective negative control ($p<0.05$; 2-fold) LFQ data as determined by MaxQuant. Sheet 2: GFP-DONSON-binding proteins enriched in the S-phase cells ($p<0.02$ & ratio>2. Q-value: quality score. Peptides: number of peptides identified. MS/MS count: number of independent spectra identified.

Supplementary Table 4 – DONSON primer sequences used in this study

Details of the DONSON primers used in this study

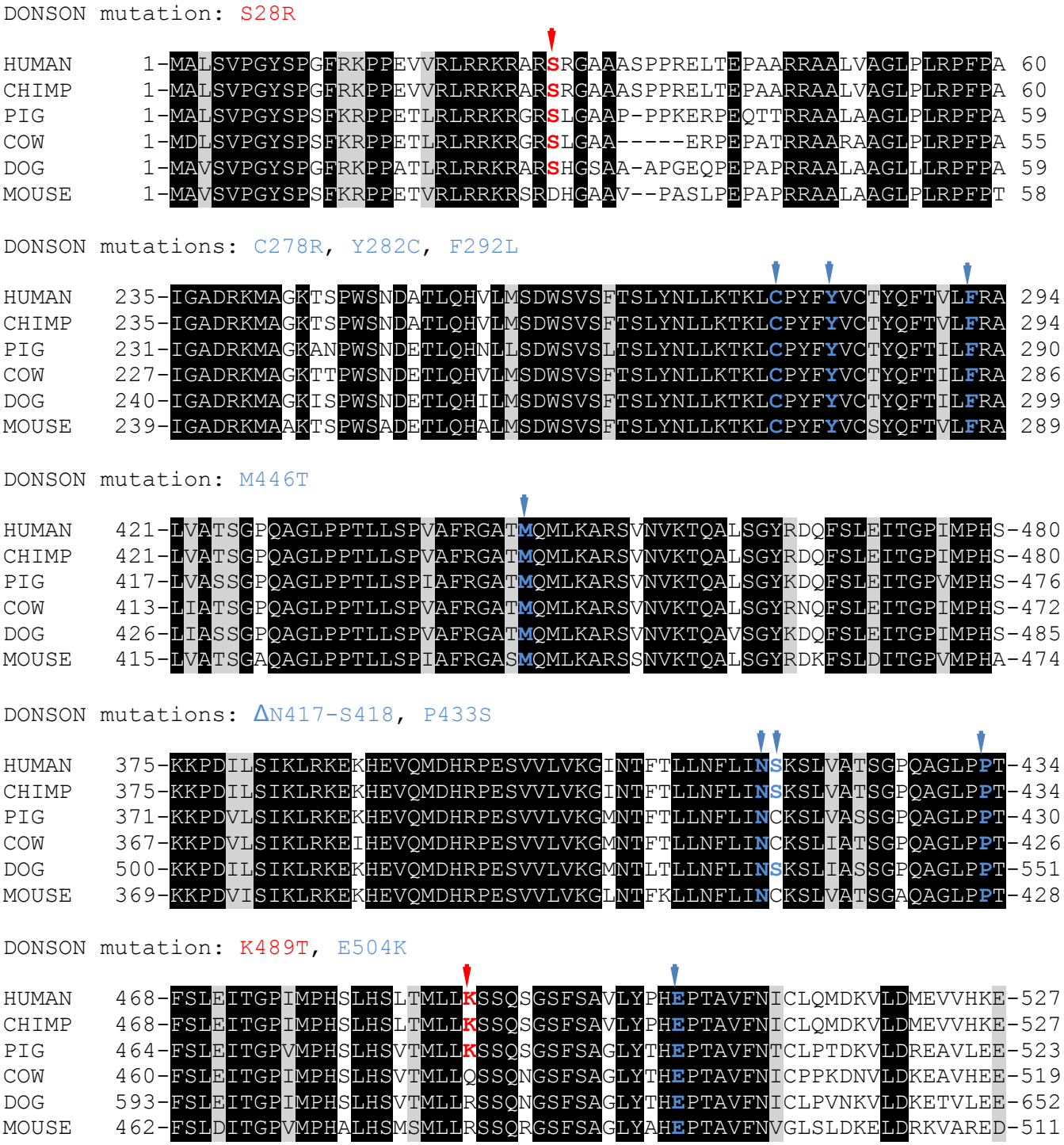

Supplementary Figure 1: Conservation of DONSON amino acids mutated in MD patients.

Amino acid alignment of DONSON protein from different species showing the degree of evolutionary conservation of disease causing DONSON point mutations, generated using Clustal Omega. Red arrows indicate the amino acid residues of DONSON mutated in MD patients. The K489T and S28R missense variants associated with the haplotype present in patients P1-7 are coloured red. All other mutations are coloured blue.

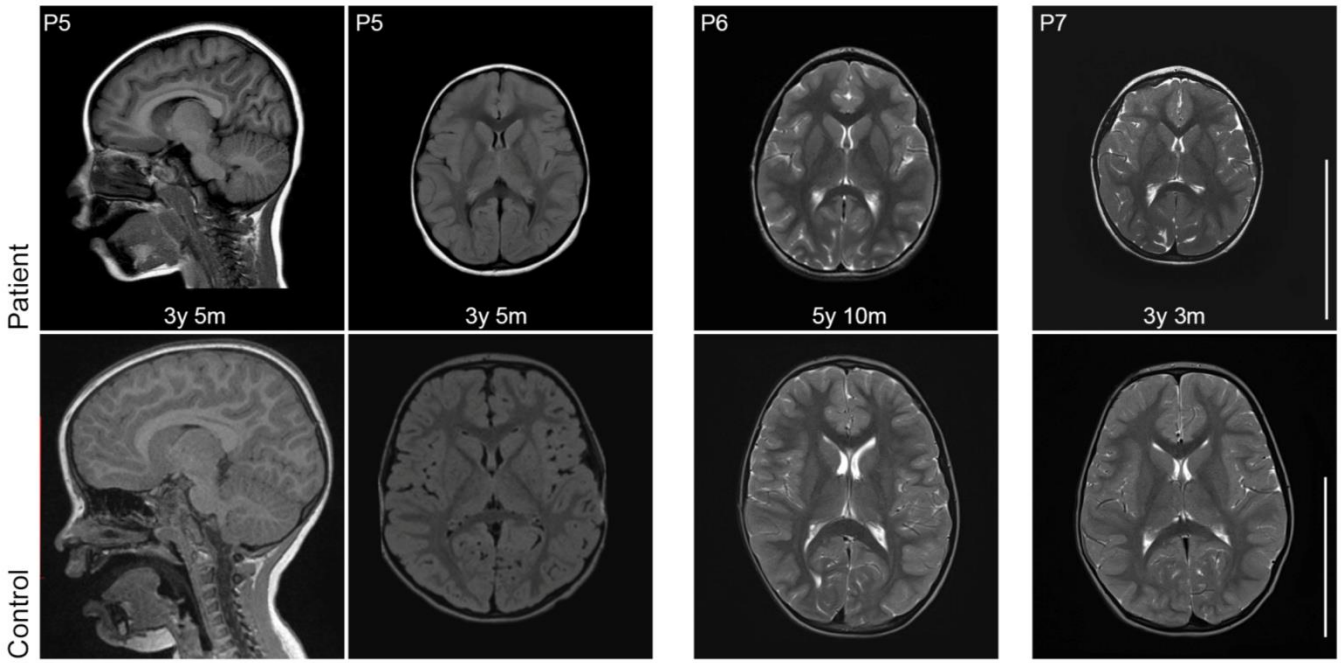

Supplementary Figure 2: Cerebral cortical size is markedly reduced with simplification of gyral folding in patients with *DONSON* mutations.

Magnetic resonance imaging T1-weighted sagittal and axial FLAIR images of patient P5, and T2-weighted sagittal and axial images of patients P6 and P7, compared with age-matched control scans of healthy individuals. Scale bars, 10 cm.

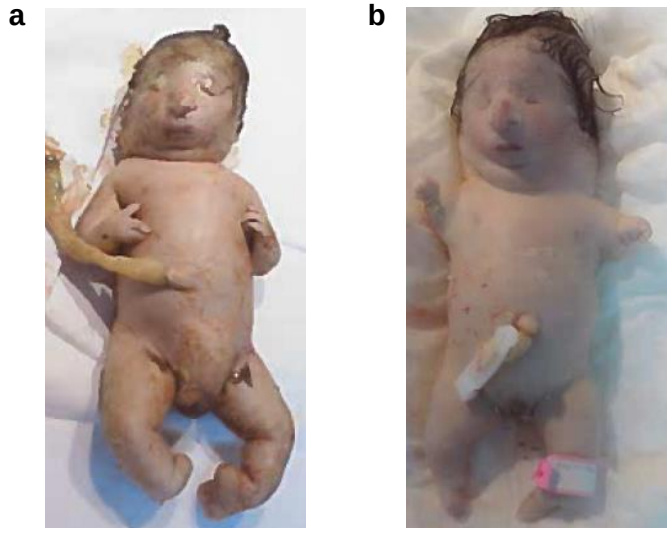

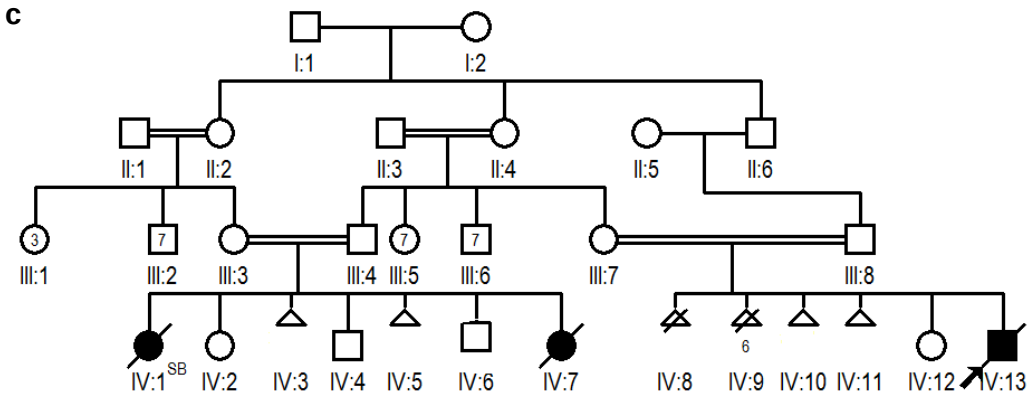

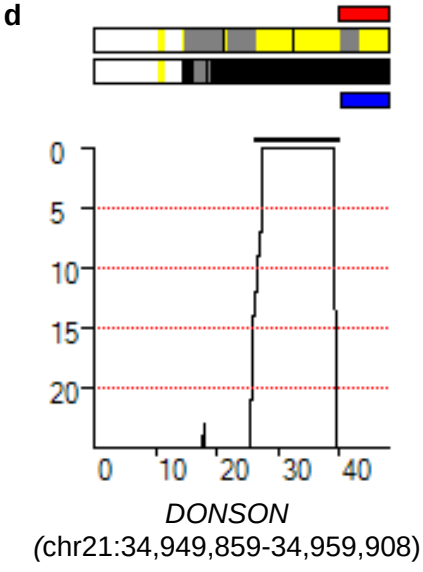

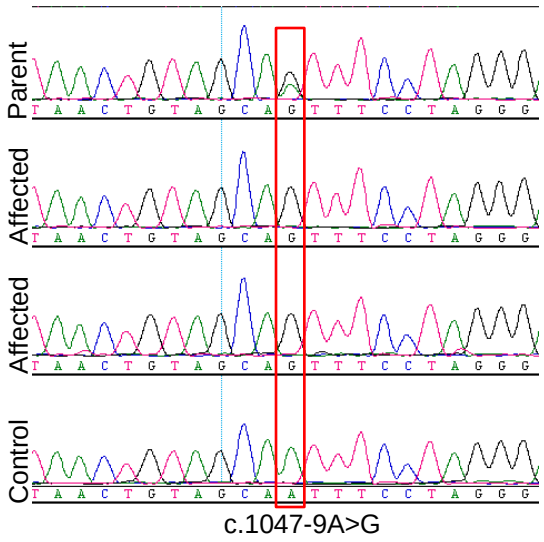

Supplementary Figure 3: Clinical and genetic characterisation of affected individuals from family P21.

(a) and **(b)** are clinical photographs of dead fetuses (P21-1 and P21-2). **(c)** Pedigree of family P21. **(d)** IBDelphi image of chromosome 21. **(e)** Chromatograms indicating the presence of the c.1047-9A>G mutation within both affected fetuses, and a parent, from family P21.

SNPs	Distance Mb	P14	P15	P16	P17	P18-1	P18-2	P18-3
RS7279441	24.1Mb	AA	AA	AA	ab	AA	AA	AA
RS1118467	24.2Mb	ab	ab	BB	AA	ab	ab	ab
1332 markers								
RS171487	29Mb	ab	BB	BB	BB	ab	ab	ab
RS2831134	29Mb	AA	AA	AA	AA	ab	ab	ab
142 markers								
RS2831813	29.8Mb	BB	BB	ab	BB	BB	BB	BB
RS4420778	29.8Mb	BB	BB	BB	BB	BB	BB	BB
519 markers								
RS2255507	32.4Mb	BB	AA	AA	BB	ab	ab	ab
RS2833282	32.4Mb	AA	AA	AA	AA	AA	AA	AA
440 markers								
RS17632819	34.4Mb	BB	ab	BB	AA	BB	BB	BB
RS2409469	34.4Mb	BB	BB	BB	BB	BB	BB	BB
67 markers								
RS17860260	34.6Mb	BB	BB	BB	BB	AA	AA	AA
RS2834167	34.6Mb	BB	BB	BB	BB	BB	BB	BB
RS2515716	34.6Mb	AA	AA	AA	AA	AA	AA	AA
33 markers								
RS2834236	34.9Mb	AA	AA	AA	AA	AA	AA	AA
DONSON	34.9Mb	AA	AA	AA	AA	AA	AA	AA
DONSON	34.9Mb	BB	BB	BB	BB	BB	BB	BB
RS2070392	35Mb	BB	BB	BB	BB	BB	BB	BB
280 markers								
RS2834657	36.2Mb	AA	AA	AA	AA	AA	AA	AA
RS2834658	36.2Mb	BB	BB	BB	BB	BB	BB	BB
RS2298352	36.2Mb	BB	BB	AA	BB	BB	BB	BB
280 markers								
RS2835192	37.3Mb	AA	AA	AA	AA	AA	AA	AA
RS11910121	37.3Mb	ab	BB	BB	BB	BB	BB	BB
326 markers								
RS2211845	39.1Mb	AA	AA	AA	BB	BB	BB	BB
RS8133218	39.1Mb	BB	BB	BB	BB	ab	ab	ab
1253 markers								
RS150792	43.4Mb	BB	BB	BB	BB	BB	BB	BB
RS150796	43.4Mb	ab	AA	ab	BB	BB	BB	BB
436 markers								
RS4819274	48Mb	BB	BB	BB	AA	BB	ab	BB
RS9637 231	48Mb	AA	AA	ab	BB	AA	ab	AA

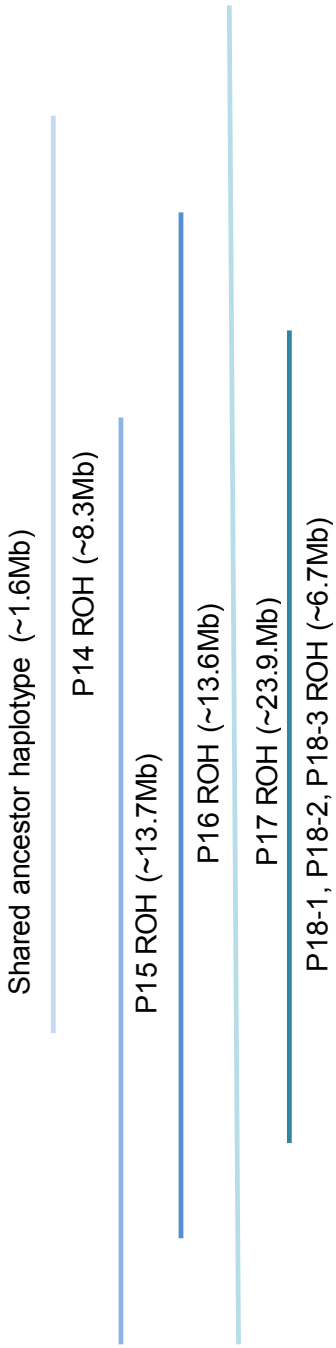

Supplementary Figure 4: Common ancestral haplotype flanking the *DONSON* locus in families P14 to P18-3.

Patients P14, P15, P16, P17, P18-1, P18-2 and P18-3 have a distant common ancestry, sharing a common ~1.6 Mb homozygous haplotype across the *DONSON* locus. Schematic of high density SNP genotyping of the *DONSON* locus in the six patients indicated above. The different families are indicated by different shades of blue. Heterozygous SNP markers delineating regions of homozygosity are shown in red. An identical haplotype of 321 SNPs is evident within the 1.6 Mb region of homozygosity in the six patients, which is consistent with a shared common ancestor (indicated by grey shading). 313 homozygous SNP markers within the 1.6 Mb regions are omitted for clarity.

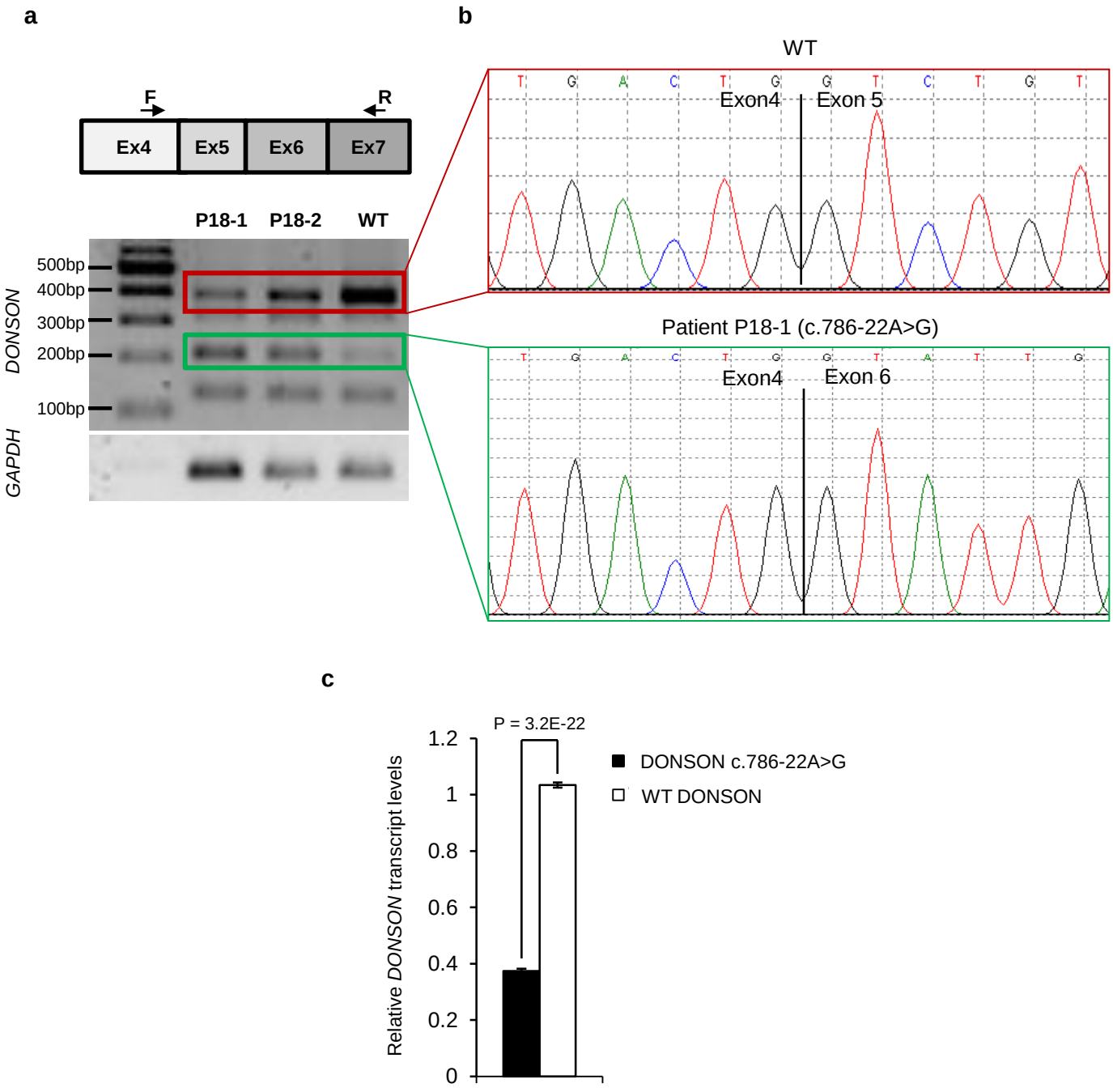

Supplementary Figure 5: The patient-associated *DONSON* intronic mutation c.786-22A>G affects mRNA splicing.

(a) Top: a schematic of *DONSON* mRNA with the position of the PCR primers (F = forward primer; R = reverse primer) indicated relative to the exons. Bottom: PCR amplification of *DONSON* exons 4-7 from cDNA derived from a WT individual or patients 18-1 and 18-2. PCR amplification of *GAPDH* was used as a control. **(b)** Sequencing electropherogram of the PCR products highlighted in (a). The red box indicates the WT sequence. The green box indicates skipping of exon 5 of *DONSON*. **(c)** Quantification of the relative amounts of the WT *DONSON* mRNA as compared to the levels of GAPDH by RT-qPCR from three normal individuals and four *DONSON* patients (n=3).

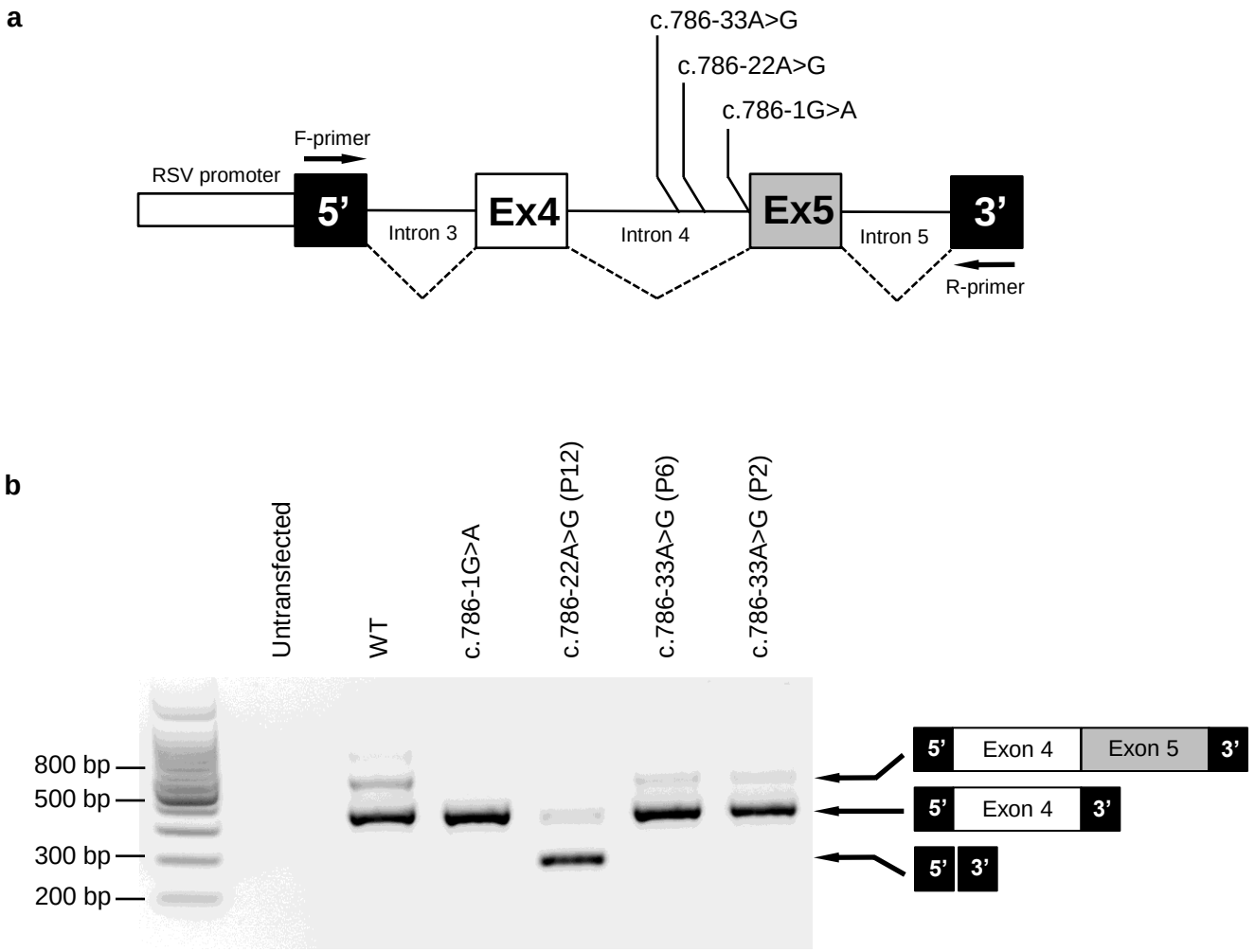

Supplementary Figure 6: The patient-associated *DONSON* intronic mutation c.786-33A>G does not affect mRNA splicing.

(a) A schematic of *DONSON* mRNA splicing mini gene reporter construct with the relative positions of the PCR primers, RSV promoter, two artificial vector-associated exons (labelled as 5' and 3') and *DONSON* exons/introns indicated. The location of the two *DONSON* intronic variants (c.786-22A>G and c.786-33A>G) relative to the intron/exon boundaries are shown. An essential splice site c.786-1G>A mutation was generated as a positive control that disrupts splicing. The position of the PCR primers (F-primer = forward primer; R-primer = reverse primer) is indicated relative to the exons. **(b)** PCR amplification of *DONSON* exons 4-5 from cDNA derived from the splicing reporter construct containing WT or the individual *DONSON* mutations. The exon content of each PCR product was verified by sequencing (indicated).

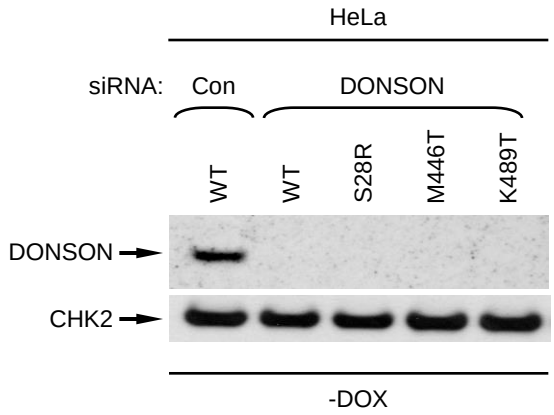

Supplementary Figure 7: Depletion of endogenous DONSON in HeLa Flp-In/T-Rex cells

Endogenous DONSON was depleted using siRNA from HeLa Flp-In/T-Rex cells expressing doxycycline-inducible GFP-tagged siRNA-resistant WT or mutant DONSON. Endogenous DONSON were detected using an anti-DONSON antibody. CHK2 was used as a loading control.

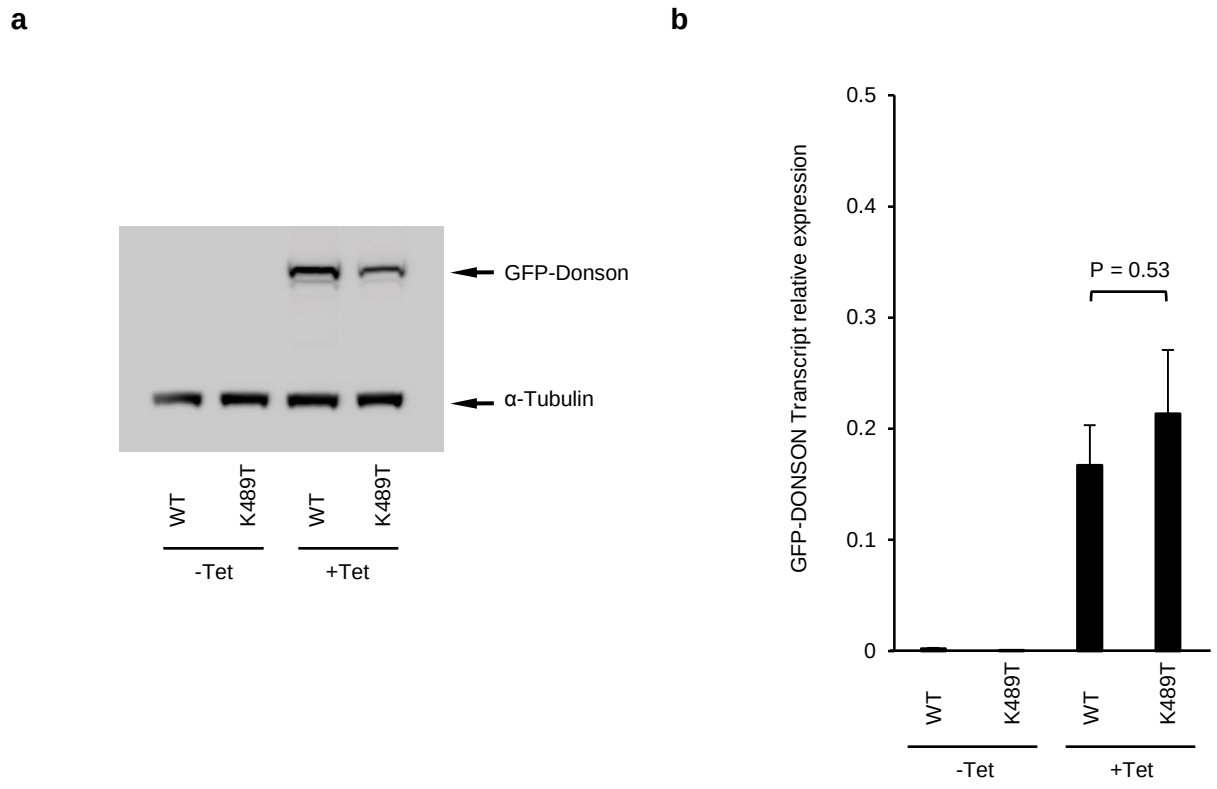

Supplementary Figure 8: Alterations in the protein level of the K489T GFP-DONSON variant are not due to reduced levels of mRNA

(a) Immunoblotting using an anti-GFP antibody demonstrates reduced protein levels of the K489T GFP-DONSON variant compared to WT GFP-DONSON (same cell lines as **Fig 2d**). '+Tet', expression induced by treatment with 1 ug/ml tetracycline for 24 h; '-Tet' uninduced. α-Tubulin was used as a loading control. **(b)** qRT-PCR analysis of GFP-DONSON transcript levels from RNA isolated from the same cell pellets as in (a). Transcript levels are expressed relative to the housekeeping gene PBGD. Data in (a) and (b) are representative of three technical replicates from two independent experiments.

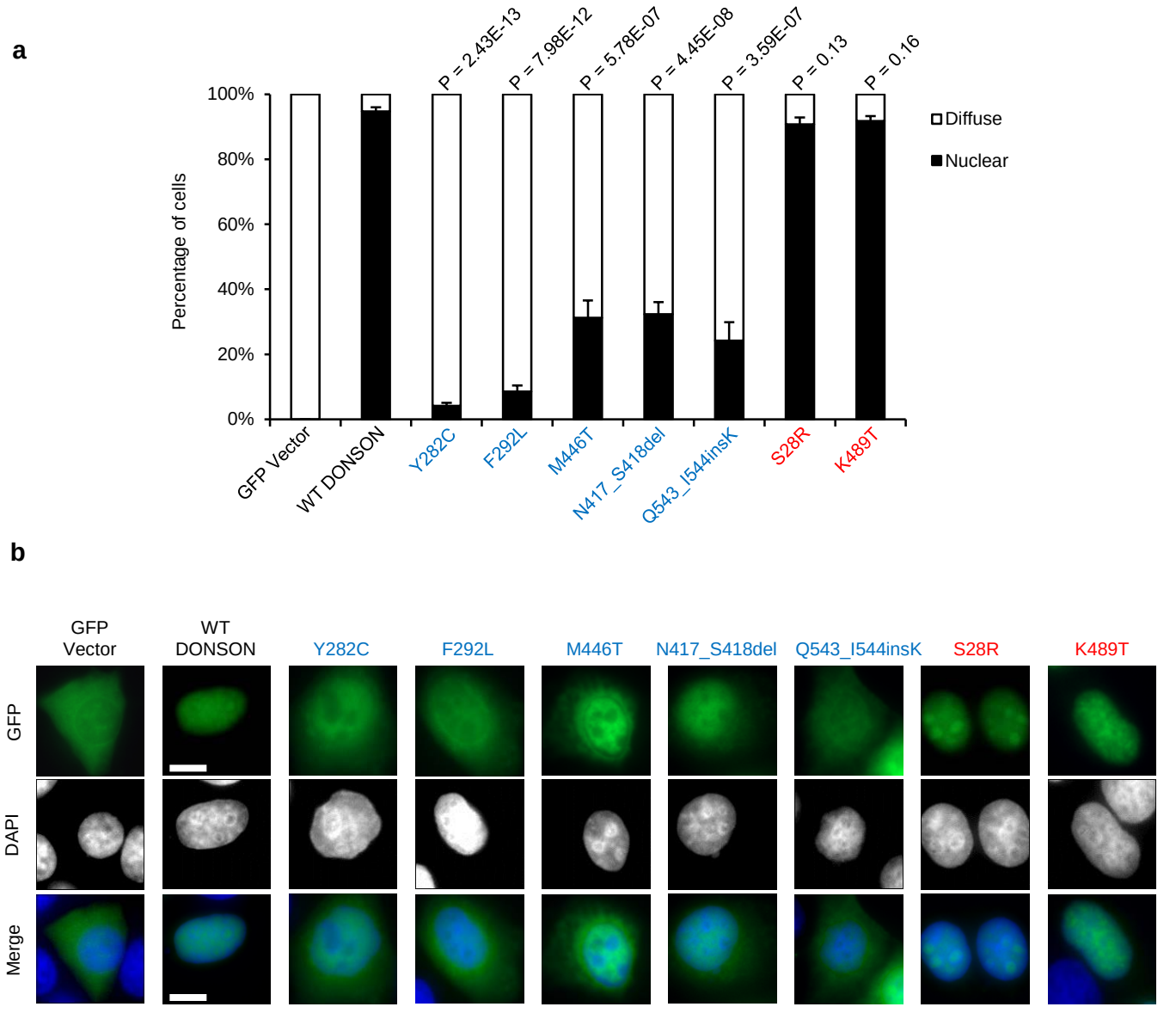

Supplementary Figure 9: The patient-associated DONSON point mutations disrupt protein sub-cellular localisation.

(a) Patient-associated point mutations in DONSON affect its subcellular localization. HeLa cells were transfected with a vector encoding either WT GFP-DONSON, or GFP-DONSON containing patient-derived mutations and fixed 24 h post-transfection. The percentages of GFP positive cells that contained either a solely nuclear GFP signal, or a diffuse pan-cellular GFP signal were quantified (n=5). Statistical differences between WT and mutated GFP-DONSON were determined by Student's t-test. **(b)** Representative images are shown. Missense mutations associated with the haplotype in patients P1 to P7 are shaded red and all other mutations are shaded blue. Scale bars; 10 µm.

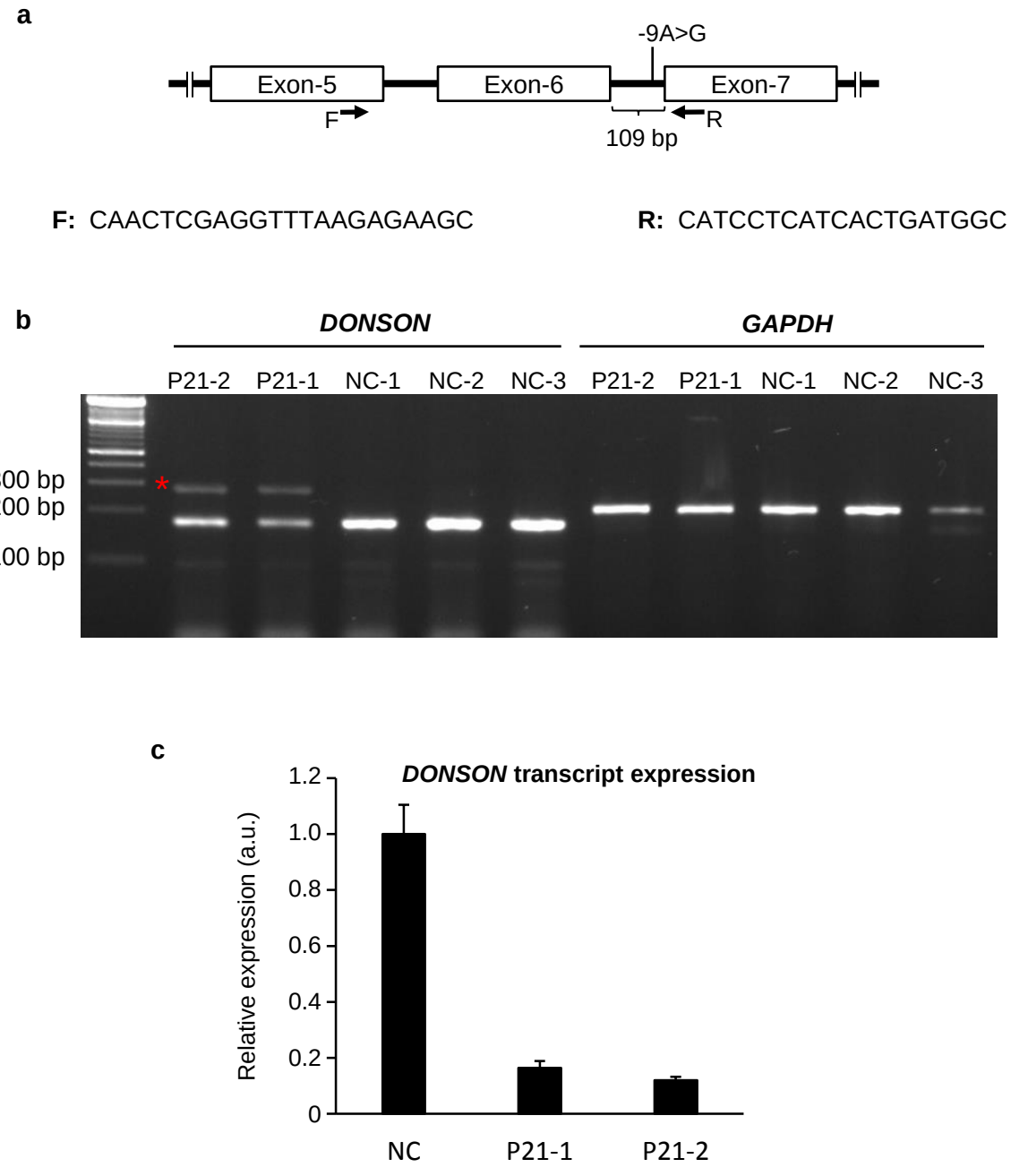

Supplementary Figure 10: The patient-associated *DONSON* intronic mutation c.1047-9A>G affects mRNA abundance.

(a) Schematic presentation of exon and intron boundaries of a region of *DONSON*. Arrows indicates primers (F; forward: and R; reverse) used for semi-quantitative RT-PCR and qRT-PCR. **(b)** Semi-quantitative RT-PCR analysis of *DONSON* transcript levels in P21-1 and P21-2 and three normal controls (NC-1, NC-2 and NC-3). Red star indicates retention of intronic region in patient amplicon. **(c)** qRT-PCR analysis of *DONSON* transcript levels, normalised to *GAPDH*, in patients P21-1, P21-2 and three normal controls (NC) (n=3). Error bars indicate standard deviation (a.u. = arbitary units).

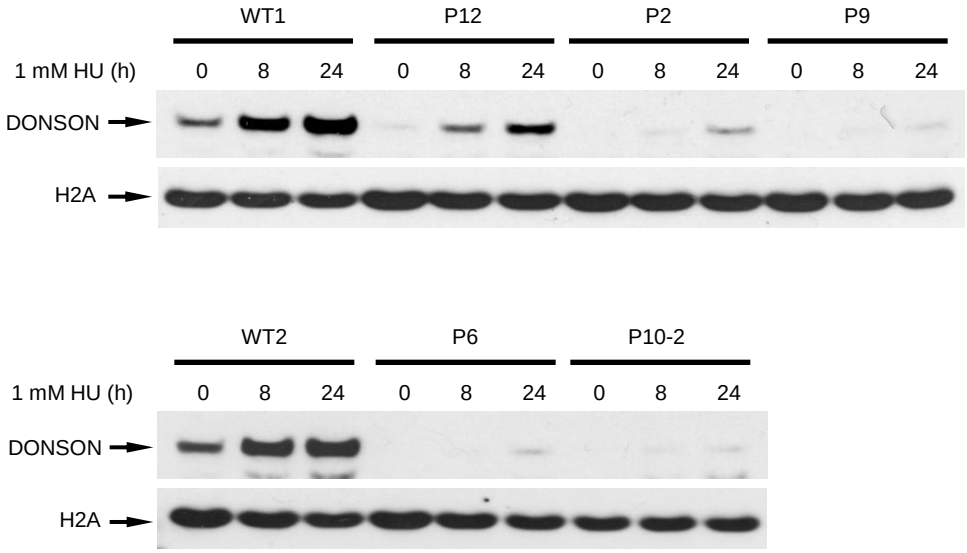

Supplementary Figure 11: Patient derived fibroblasts retain residual levels of DONSON protein.

Immunoblotting of cell extracts from patient derived fibroblast cell lines treated with HU for the indicated times. H2A was used as a loading control.

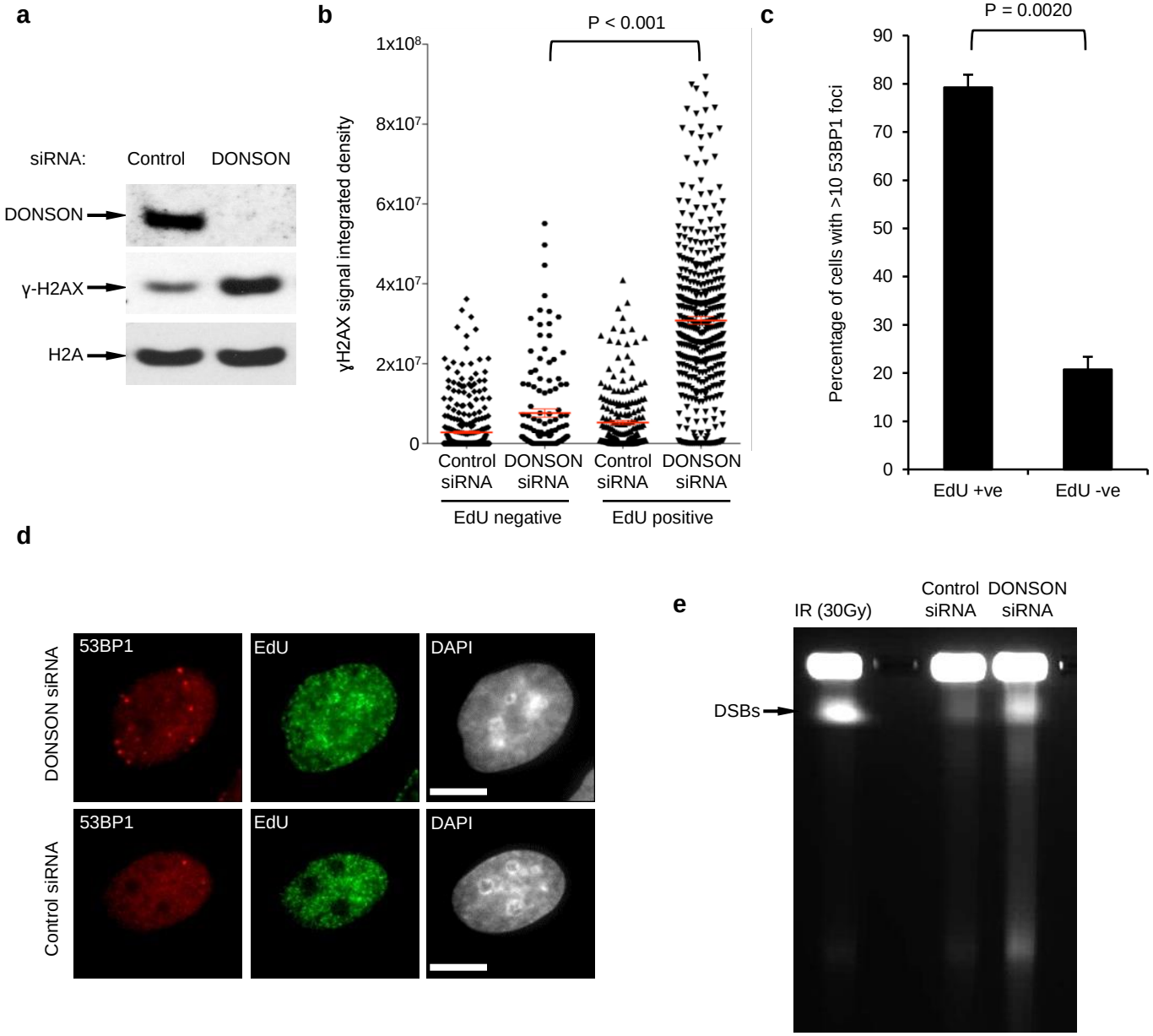

Supplementary Figure 12: Depletion of DONSON gives rise to increased spontaneous DNA damage in replicating cells.

(a) Knockdown of DONSON results in increased levels of phosphorylated H2AX. HeLa cells were transfected with control or DONSON siRNA, harvested 72 h post-transfection and extracts subjected to SDS-PAGE and immunoblotting using the antibodies indicated (n=3). **(b-e)** DONSON depletion causes DNA double strand breaks in replicating cells. **(b)** DONSON-depleted cells were seeded onto coverslips and incubated with 10 μM EdU for 10 min before harvesting. Cells were then pre-extracted, fixed and stained with an antibody to γH2AX. EdU was visualised using the Click-iT-Alexa-488 Imaging Kit. The intensity of γH2AX immunostaining in >100 EdU positive cells and >50 EdU negative cells were quantified per cell line per condition per experiment (n=2). **(c)** Quantification of the percentage of EdU positive and negative cells with >10 53BP1 foci in cells without DONSON. A minimum of 300 cells were counted per sample per independent experiment. (n=3). **(d)** Representative images for (c) Scale bars; 10 μm. **(e)** Pulsed-field gel electrophoresis was used to detect the presence of DNA double strand breaks (DSBs) in cells from (a). As a positive control, HeLa cells were irradiated with 30 Gy of ionising radiation (IR) and harvested 1 h later.

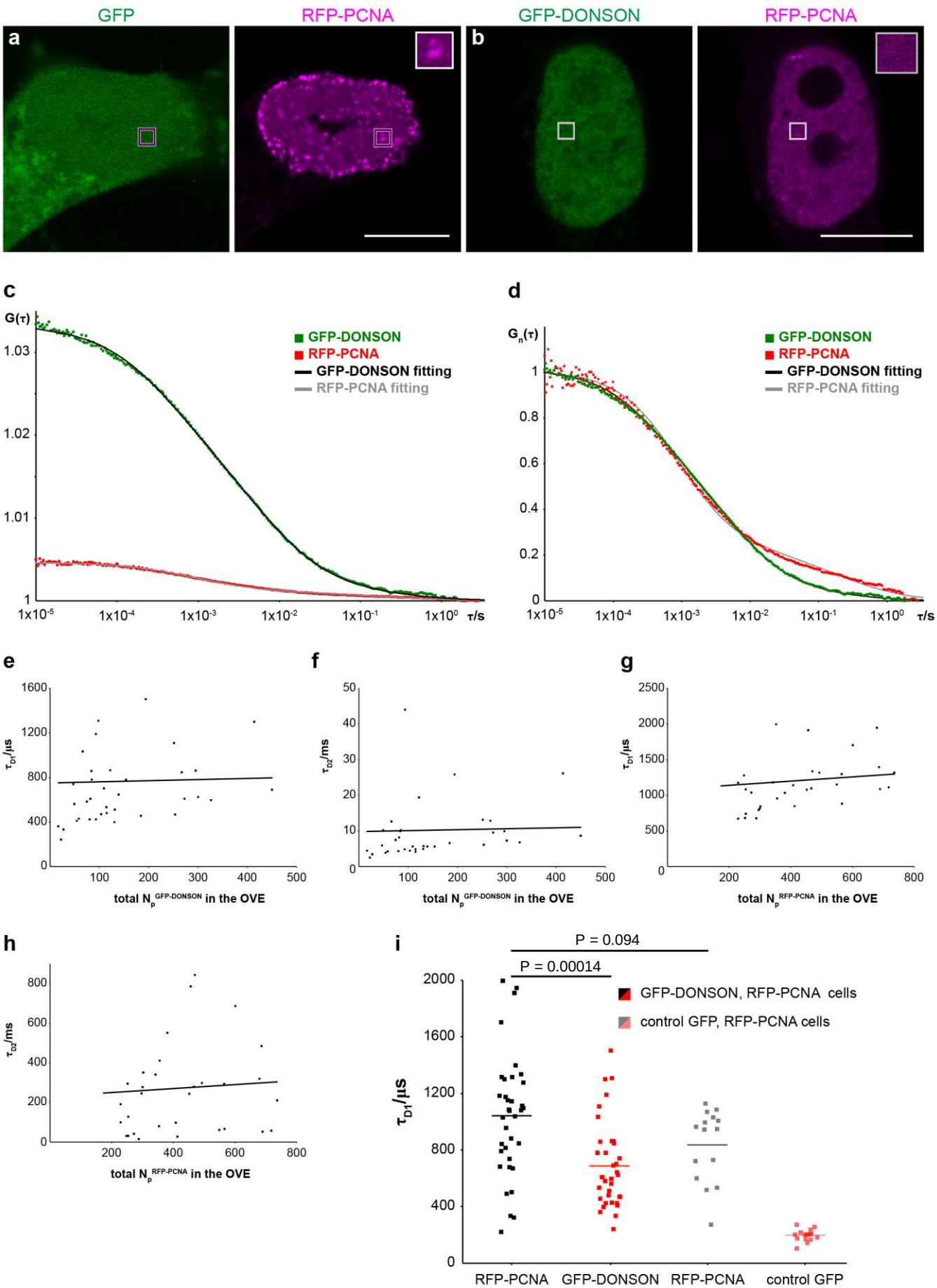

Supplementary Figure 13: Fluorescence Cross-Correlation Spectroscopy of GFP-DONSON and RFP-PCNA. See next page for legend.

Supplementary Figure 13: Fluorescence Cross-Correlation Spectroscopy of GFP-DONSON and RFP-PCNA.

Fluorescence Cross-Correlation Spectroscopy (FCCS) is a method used to analyse the degree of interaction of two differently coloured fluorescent proteins randomly diffusing through a fixed volume. Control measurements for GFP, GFP-DONSON and RFP-PCNA from FCS(fluorescence Correlation Spectroscopy)/FCCS experiments. **(a, b)** Representative confocal images of HeLa cells expressing **(a)** GFP and RFP-PCNA in S-phase, and **(b)** GFP-DONSON and RFP-PCNA in non-S phase. The purple and grey boxes indicate regions representative of those in which FCS/FCCS measurement were performed. Scale bars, 10 μm. **(c)** Average Auto-Correlation Curves (ACCs) of measurements of GFP-DONSON and RFP-PCNA in replication foci (displayed in **Fig. 4e, f**). High concentrations of both RFP-PCNA and GFP-DONSON (3 ± 1.2 μM and 1.1 ± 0.8 μM, respectively, n=36) were measured by FCS at replication foci, even in cells displaying low average amounts of PCNA and DONSON. For cross-correlation analysis, (**Fig. 4f**) only measurements from cells displaying similar levels of RFP-PCNA, and GFP-DONSON or GFP, were compared. Fitting was performed using a two-component model with triplet formation (see **Supplementary Note 1**). **(d)** Average FCS measurements normalized to the same amplitude revealed a marked difference in the mobility of the bound fraction of each protein (represented by the slow component in the ACCs, with PCNA displaying slower movement, as would be expected from a protein encircling DNA), which can be observed by the shift of the RFP-PCNA ACC to longer characteristic times. We determined $\tau_{D_1}^{RFP-PCNA} = 1041 \pm 430\,\mu s$, $\tau_{D_2}^{RFP-PCNA} = 221 \pm 225\,ms$, $\tau_{D_1}^{GFP-DONSON} = 688 \pm 303\,ms$ and $\tau_{D_2}^{GFP-DONSON} = 24 \pm 34\,ms$ (n=36) in GFP-DONSON expressing cells. **(e-h)** Characteristic decay times τ_{D_1} and τ_{D_2} are not significantly altered upon concentration increase of total GFP-DONSON and RFP-PCNA molecules, as evident from $\tau_{D_1} = f\,(N_p)$ and $\tau_{D_2} = f\,(N_p)$, where N_p is the average number of molecules of GFP-DONSON and RFP-PCNA and τ_{D_1}, τ_{D_2} the diffusion times of the unbound and bound fractions, indicating that the observed fluorescence intensity fluctuations are generated by diffusion. **(i)** Comparison of the characteristic decay times τ_{D_1}(fast FCS component, when fitted with a two-component model for three-dimensional diffusion and triplet formation) of RFP-PCNA and GFP-DONSON (n=36 measurements) or control GFP (n=15 measurements). RFP-PCNA showed considerably slower diffusion of the fast component than GFP-DONSON or control GFP, but no significant differences in its mobility were observed between cells expressing GFP-DONSON or control GFP (Student's unpaired two-tailed t-test between GFP-DONSON and RFP-PCNA, p=0.00014; and between RFP-PCNA across the two cell lines, p=0.094). Horizontal lines denote the average of measurements for each condition.

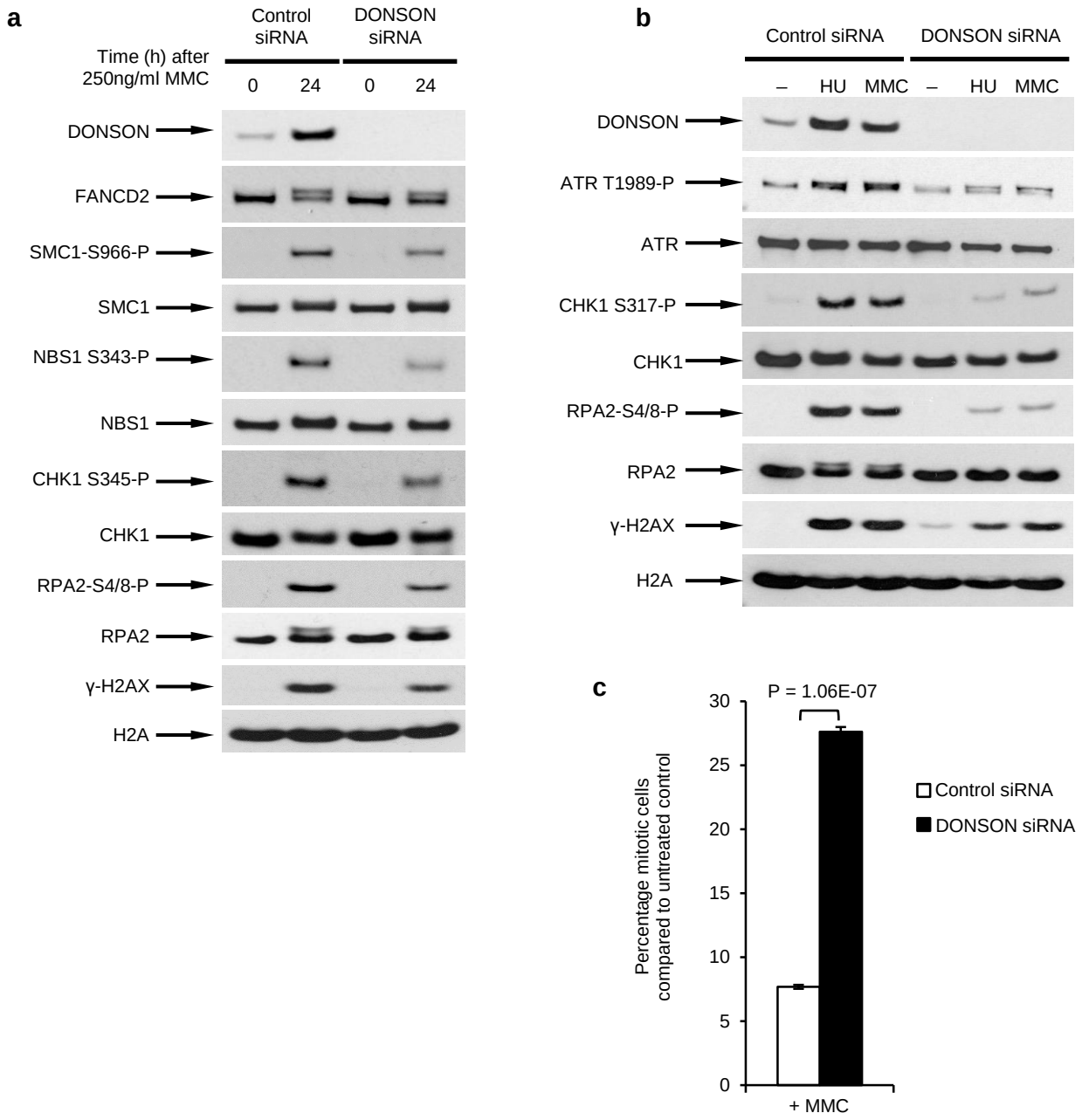

Supplementary Figure 14: Reduced ATR-CHK1-dependent signalling and defective activation of the G2/M checkpoint in DONSON-depleted cells following replication stress treatment

(a) Cells lacking DONSON exhibit defective or delayed ATR auto-phosphorylation in response to replication stress. HeLa cells transfected with either control or DONSON siRNA were exposed to 1 mM HU or 250 ng/ml MMC for 24 h, and subjected to immunoblotting using the indicated antibodies (n=2). **(b)** Cells lacking DONSON fail to efficiently activate the ATR-dependent replication stress response following exposure to MMC. Whole cell extracts of HeLa cells transfected with either control or DONSON siRNA were subjected to immunoblot analysis using the indicated antibodies following treatment with 250 ng/ml MMC for 24 h. **(c)** The percentage of mitotic cells in cells from (a) was determined by flow cytometry using antibodies to phosphorylated histone H3-Ser10 as a marker of mitotic cells. Data represents the mean of three independent experiments.

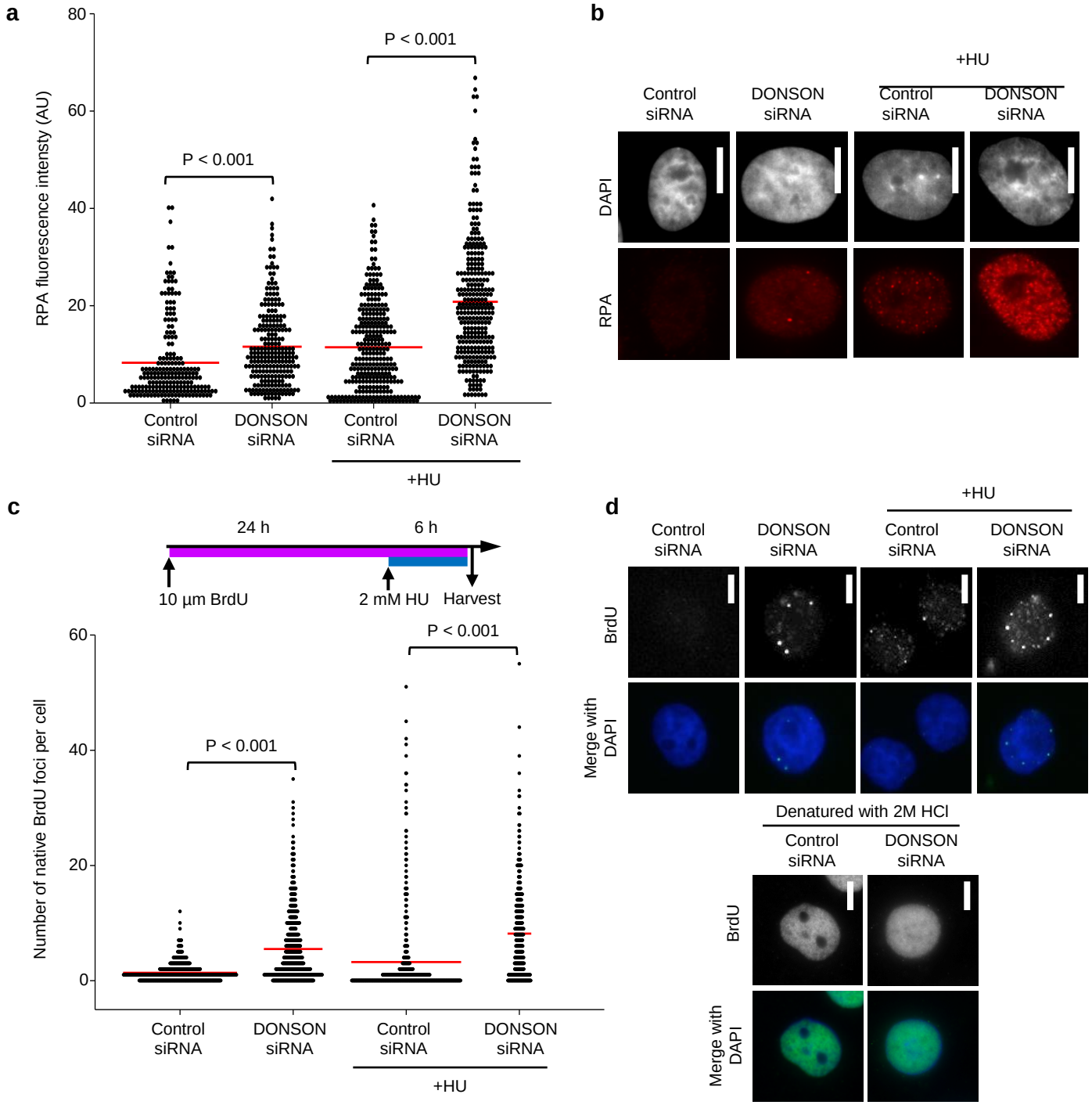

Supplementary Figure 15: Increased levels of RPA-coated ssDNA in DONSON-depleted cells following treatment with HU

Exposure of cells lacking DONSON to HU induces increased levels of RPA coated ssDNA. **(a-b)** HeLa cells transfected with either control or DONSON siRNA were exposed to 1 mM HU for 24 h, immunostained with antibodies specific to RPA2 and analysed by fluorescence microscopy. Fluorescence intensity per nucleus was quantified using ImageJ. Lines denote mean values from two independent experiments. Representative images are shown in **(b)**. **(c-d)** Native BrdU foci formation in HeLa cells transfected with the indicated siRNAs was analysed by fluorescence microscopy. The cells were treated as detailed in the schematic (top), and immunostained with antibodies to BrdU. Foci formation was quantified using ImageJ (n=3). **(d)** Representative images are shown. As a control for BrdU incorporation, cells were treated with 2 M HCl to denature DNA prior to addition of the BrdU antibody. Scale bars; 10 µm.

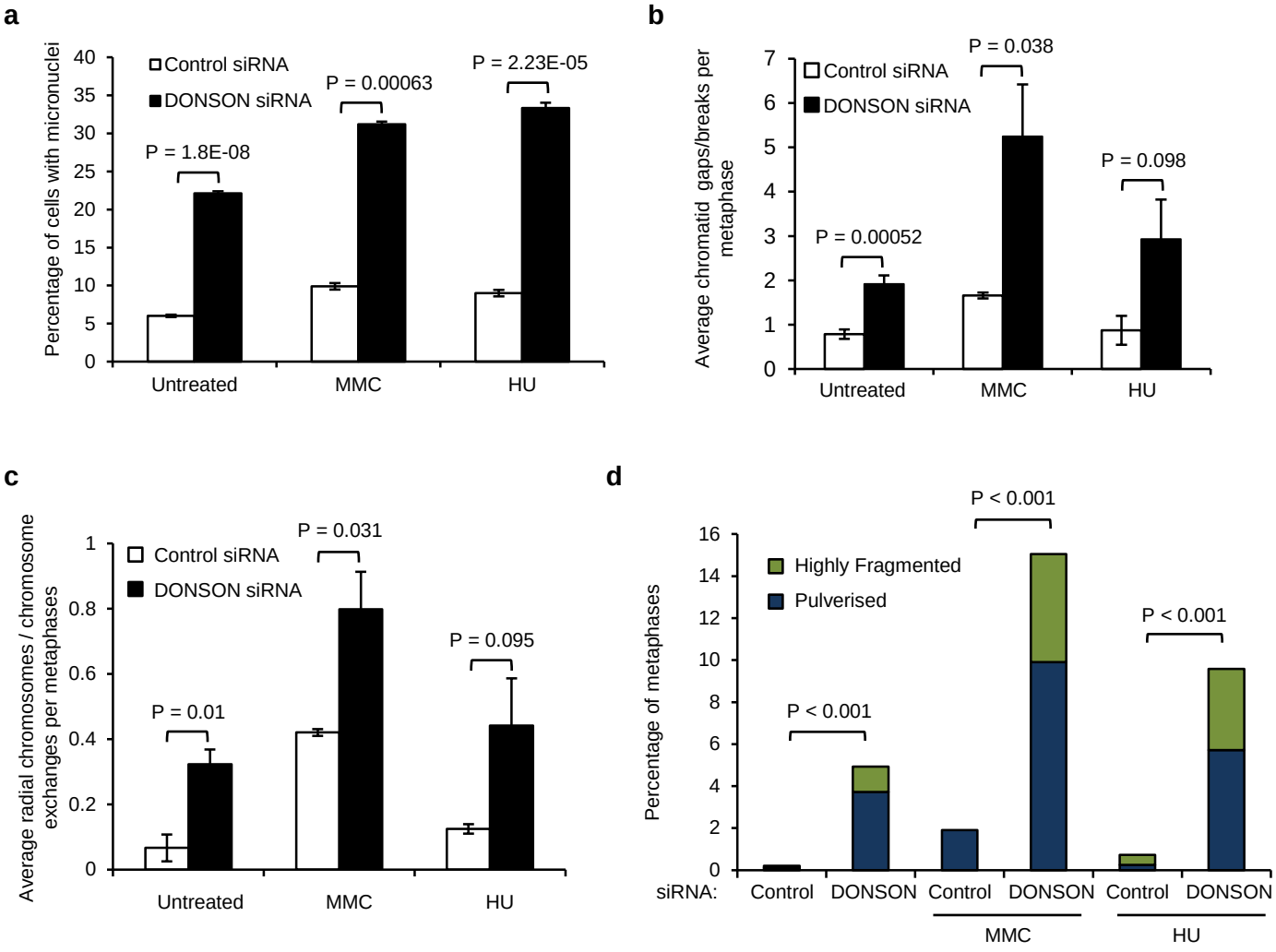

Supplementary Figure 16: Replication stress exacerbates genome instability in DONSON deficient cells.

Exposure of cells lacking DONSON to HU or MMC exacerbates micronuclei formation and chromosome breakage. **(a)** Micronuclei formation in HeLa cells transfected with either control or DONSON siRNA following exposure to either 4mM HU for 6 h, followed by 24 h recovery, or 50ng/ml MMC for 24 h was assessed using fluorescence microscopy (n=3). **(b)** Quantification of the chromatid gaps/breaks in metaphases from control or DONSON siRNA transfected HeLa cells following exposure to HU or MMC as in (a). At least 50 metaphases per experiment were counted (n=3). **(c)** Quantification of chromosome exchanges and radial chromosomes in metaphases from control or DONSON siRNA transfected HeLa cells following exposure to HU or MMC as in (a). At least 50 metaphases per experiment were counted (n=3). **(d)** Quantification of metaphases from control or DONSON siRNA transfected HeLa cells, containing highly fragmented or pulverised metaphases following exposure to HU or MMC as in (a) (n=3).

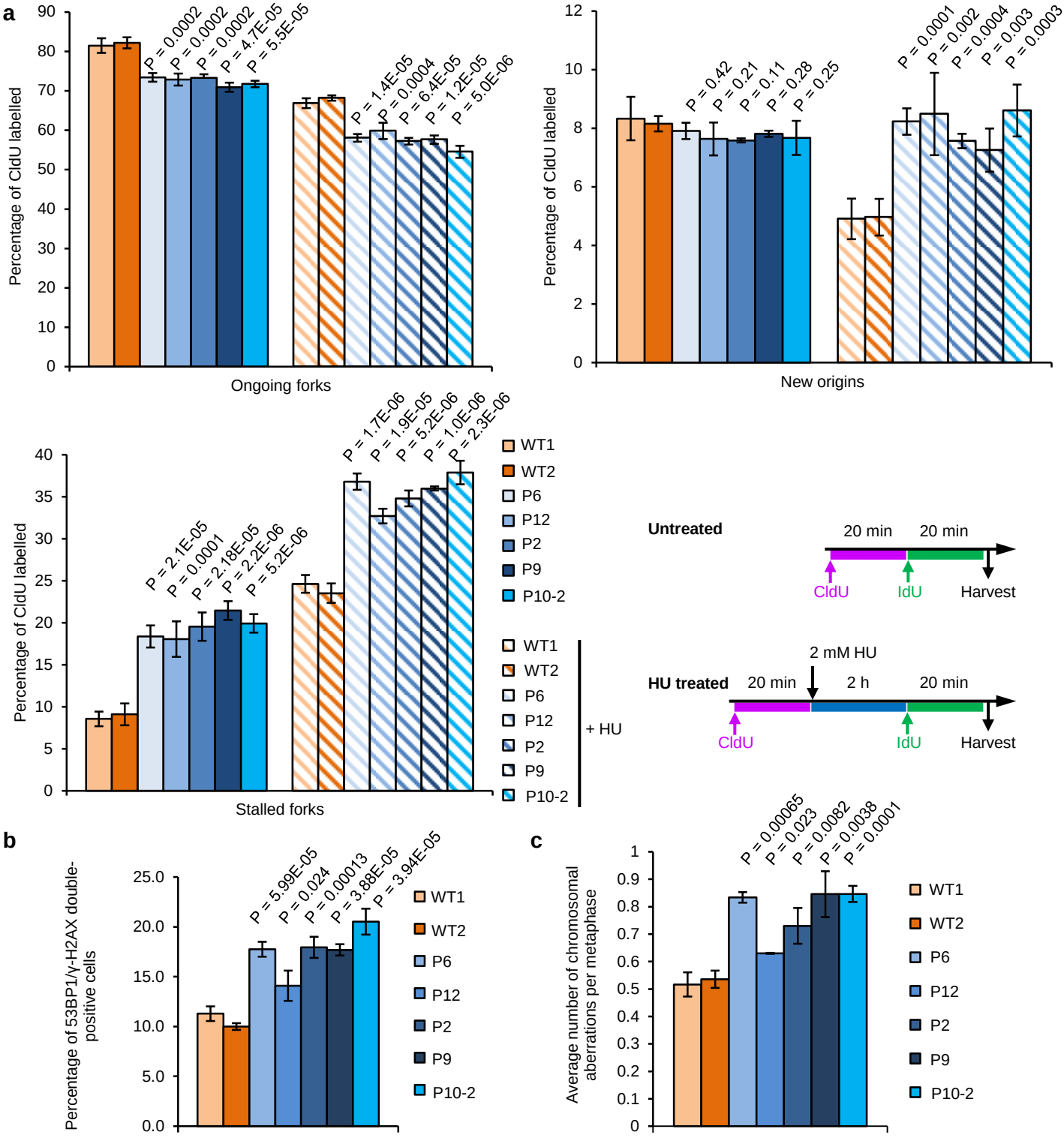

Supplementary Figure 17: Cells from patients with hypomorphic *DONSON* mutations exhibit genome instability and replication fork abnormalities that are exacerbated by replication stress.

(a) Mutation of DONSON results in replication fork instability that is exacerbated by replication stress. Patient derived fibroblasts were pulsed for 20 min with CldU, exposed to 2 mM HU for 2 h, and then pulsed with IdU for 20 min. DNA fibres were quantified, and the percentage of ongoing forks, new origin firing and stalled forks are displayed (n=3). Bottom right: Schematic of DNA fibre analysis. **(b)** DONSON patient derived fibroblasts exhibit elevated levels of spontaneous 53BP1/γH2AX foci. Patient derived fibroblasts were immunostained with antibodies to 53BP1 and γH2AX, and the percentage of cells with 53BP1/γH2AX foci were quantified (n=3). **(c)** Cells from DONSON patients exhibit spontaneous chromosomal instability. Chromosomal aberrations in patient derived fibroblasts were quantified. (n=3).

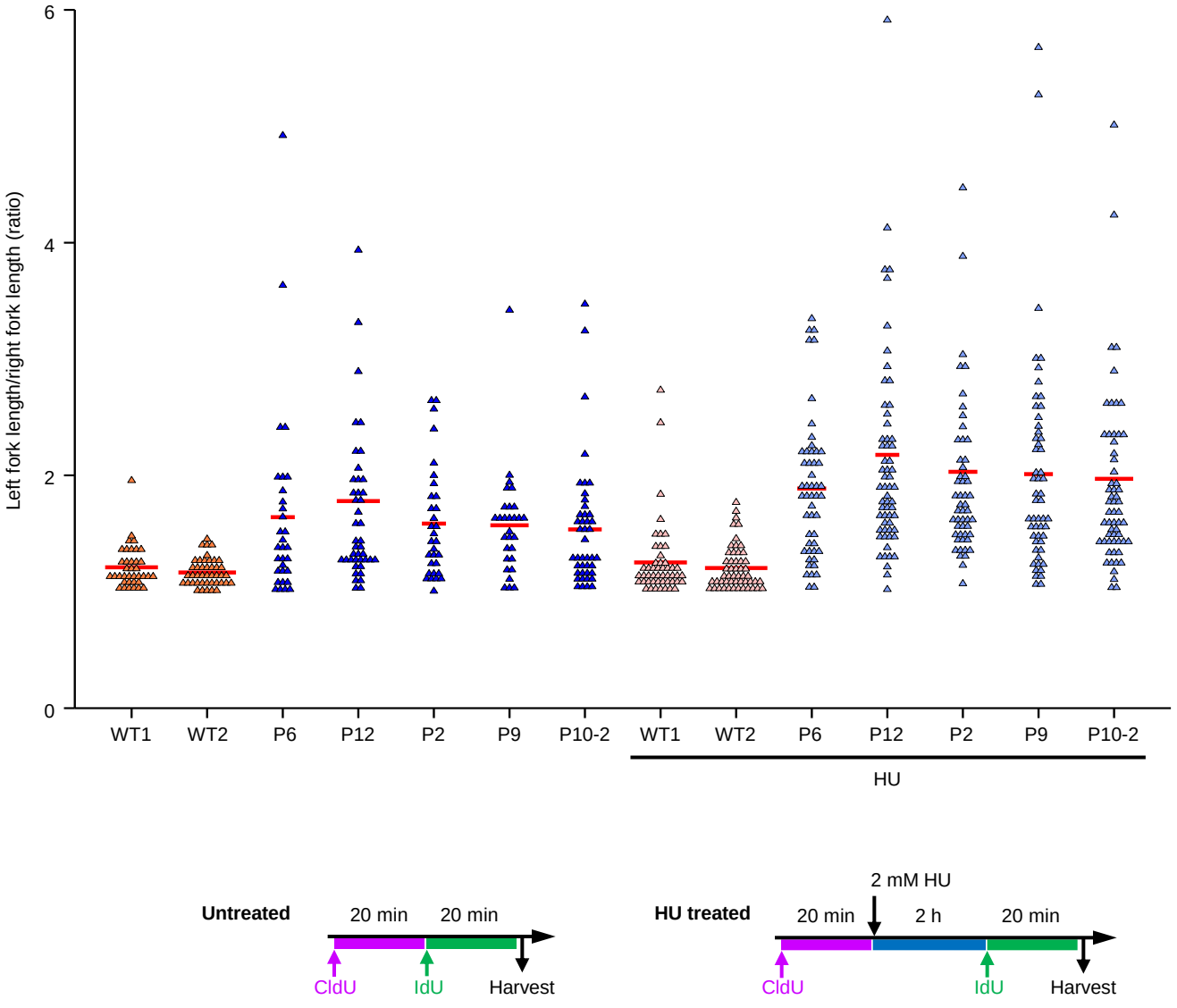

Supplementary Figure 18: Cells from patients with hypomorphic *DONSON* mutations exhibit increased replication fork instability

Quantification of DNA replication fork asymmetry in *DONSON* mutant patient-derived fibroblasts. The plot indicates the ratio of left/right fork track lengths of bidirectional replication forks. The red lines denote the median ratio (n=3). Bottom: Schematic of DNA fibre analysis.

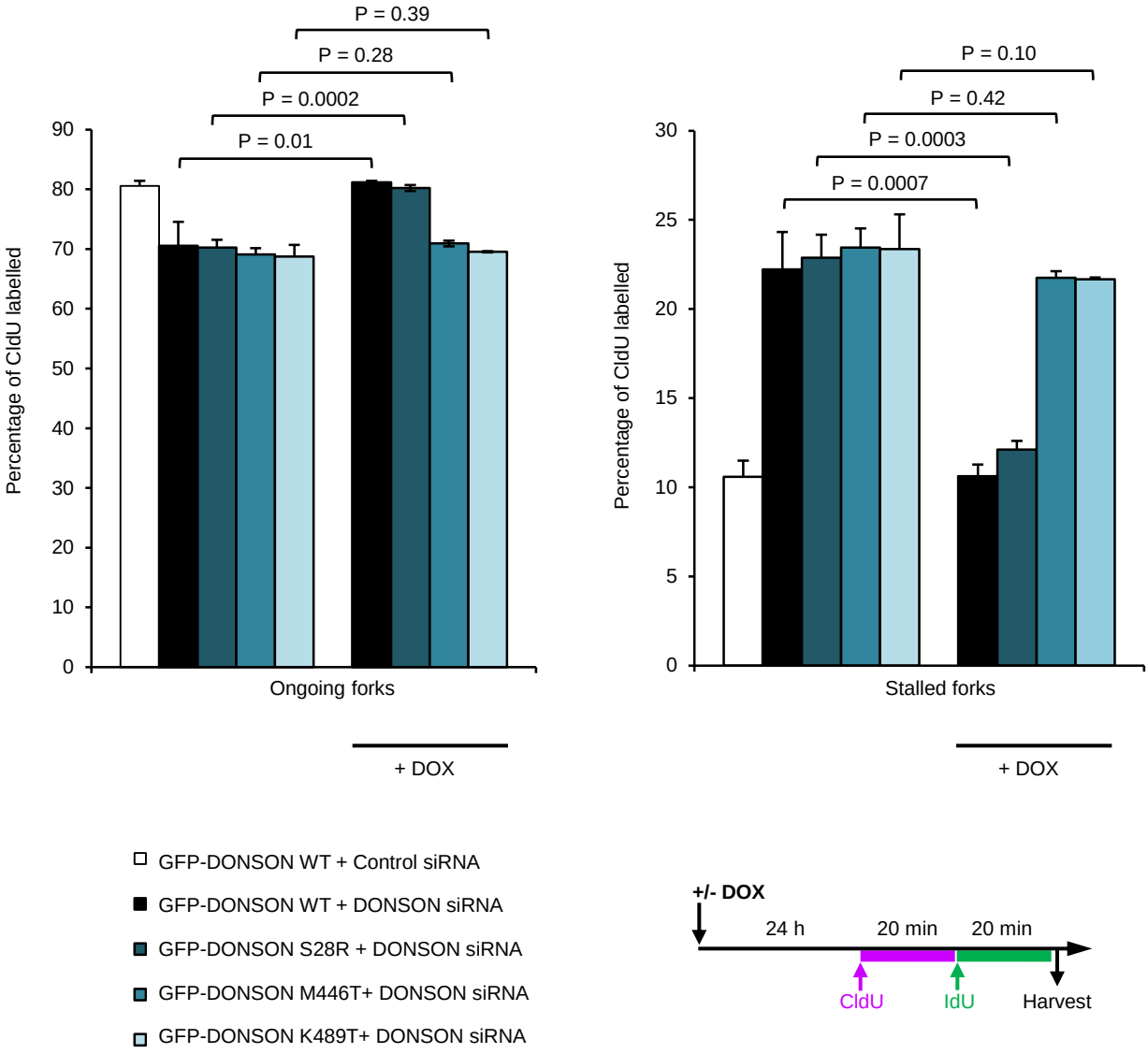

Supplementary Figure 19: The patient-derived M446T and K489T mutations fail to correct the replication fork instability associated with DONSON depletion.

HeLa Flp-In/T-Rex cells from (**Fig 2d**) expressing GFP-tagged WT or mutant DONSON under the control of a doxycycline-inducible promoter were transfected with DONSON siRNA. 48 h post-transfection, 1 µg/ml doxycycline was added for 24 h. The cells were pulsed with CldU for 20 min, followed by IdU for 20 min. DNA fibres were quantified, and the percentage of ongoing forks and stalled forks are displayed (n=2). '+DOX' indicates the addition of doxycycline 24 h prior to incubation with the thymidine analogues. Bottom: Schematic of DNA fibre analysis.

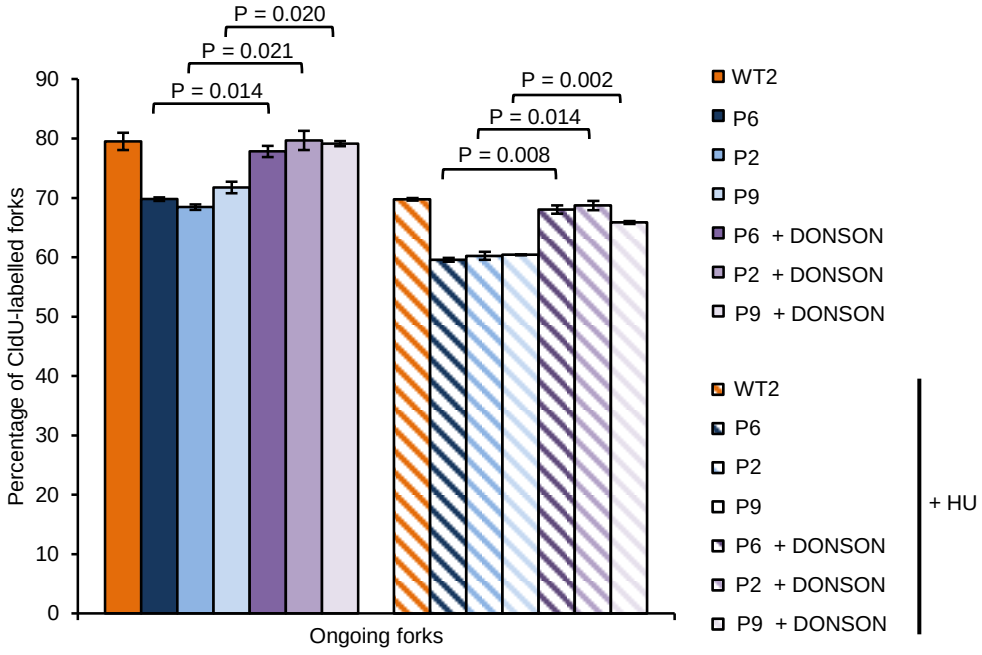

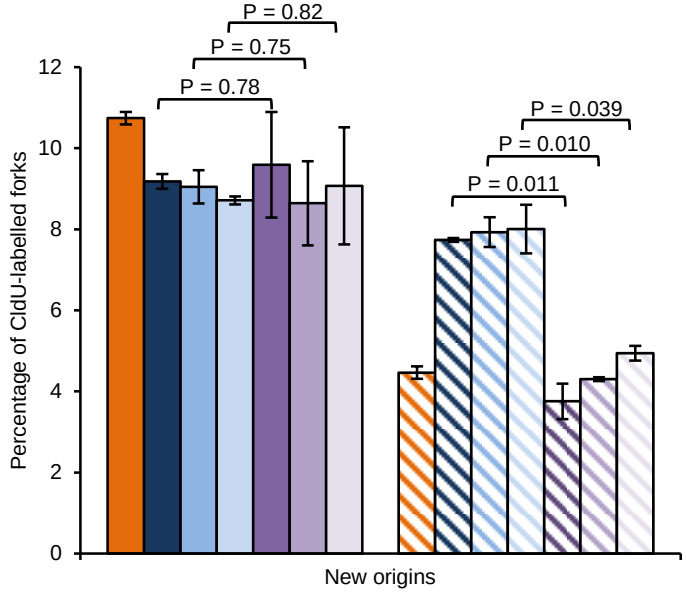

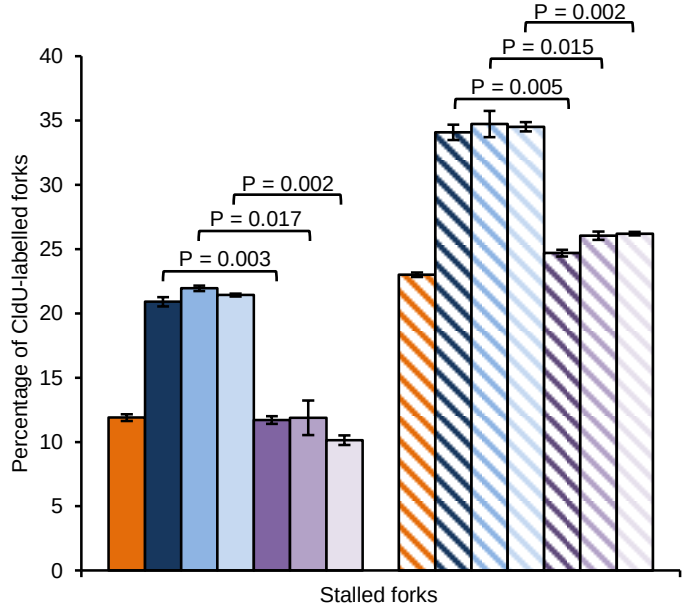

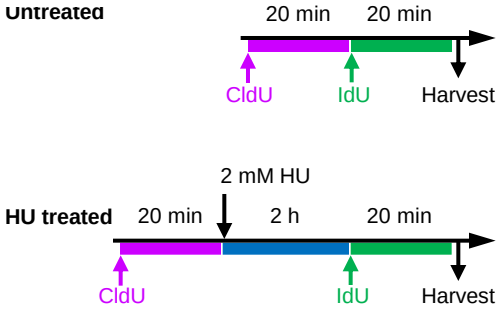

Supplementary Figure 20: Re-expression of WT *DONSON* in patient derived fibroblasts restores replication fork stability.

DNA fibre analyses in hTERT-immortalised DONSON patient fibroblasts complemented with a retrovirus either containing human WT *DONSON*, or an empty vector from (**Fig 7**). Complemented fibroblasts were pulsed with CldU, exposed to 2 mM HU for 2 h where indicated, and then pulsed with IdU. The percentage of ongoing replication forks, new origin firing and stalled forks were quantified (n=3 experiments). Quantification of new origin firing and stalled forks presented in (**Fig 7d**) have been included here for comparison. Right: Schematic of DNA fibre analysis.

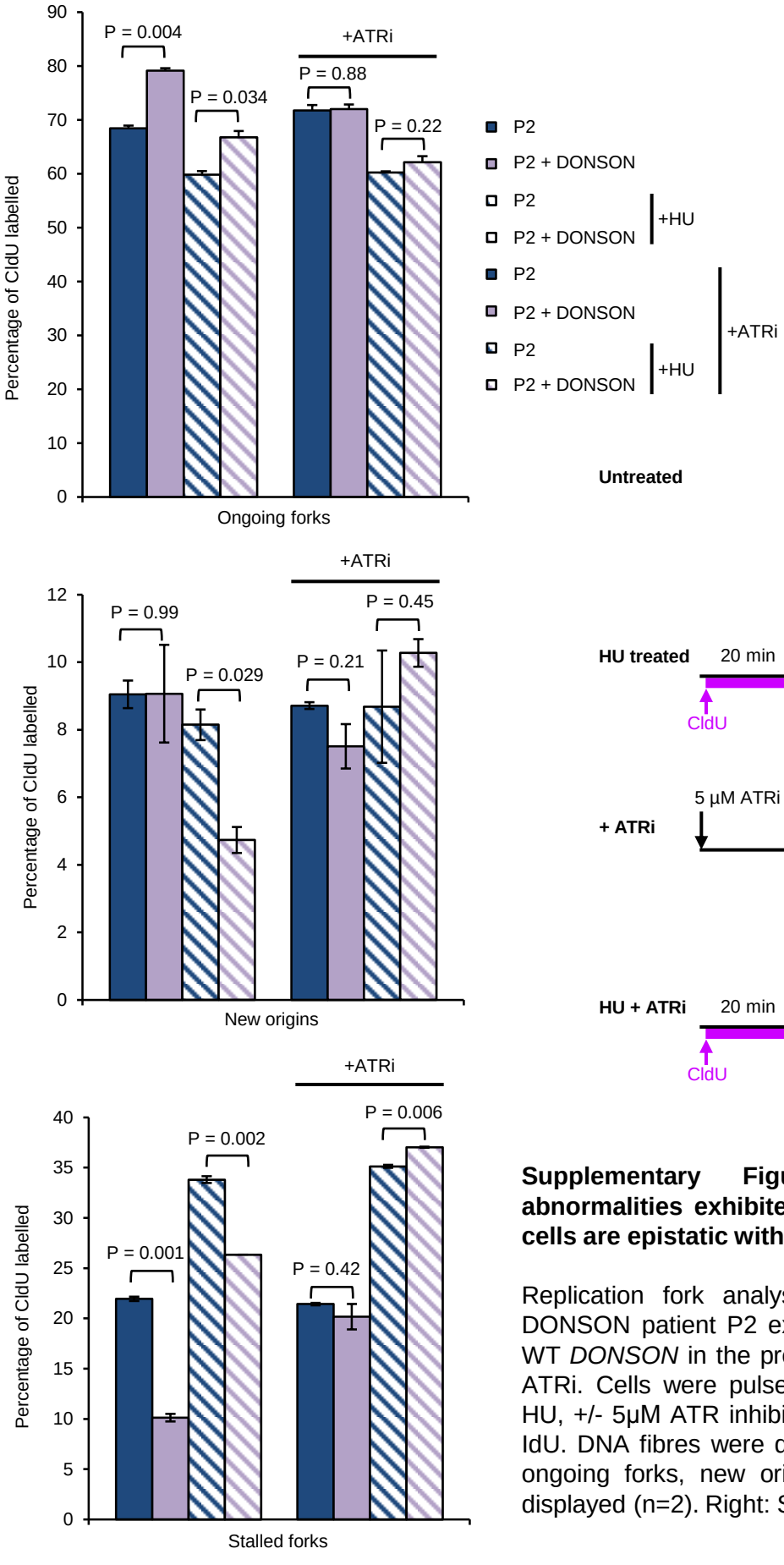

Supplementary Figure 21: The replication abnormalities exhibited by *DONSON* mutant patient cells are epistatic with ATR inhibition.

Replication fork analysis of fibroblasts derived from DONSON patient P2 expressing either empty vector or WT *DONSON* in the presence or absence of HU and/or ATRi. Cells were pulsed with CldU, exposed to 2 mM HU, +/- 5µM ATR inhibitor for 2 h, and then pulsed with IdU. DNA fibres were quantified, and the percentage of ongoing forks, new origin firing and stalled forks are displayed (n=2). Right: Schematic of DNA fibre analysis.

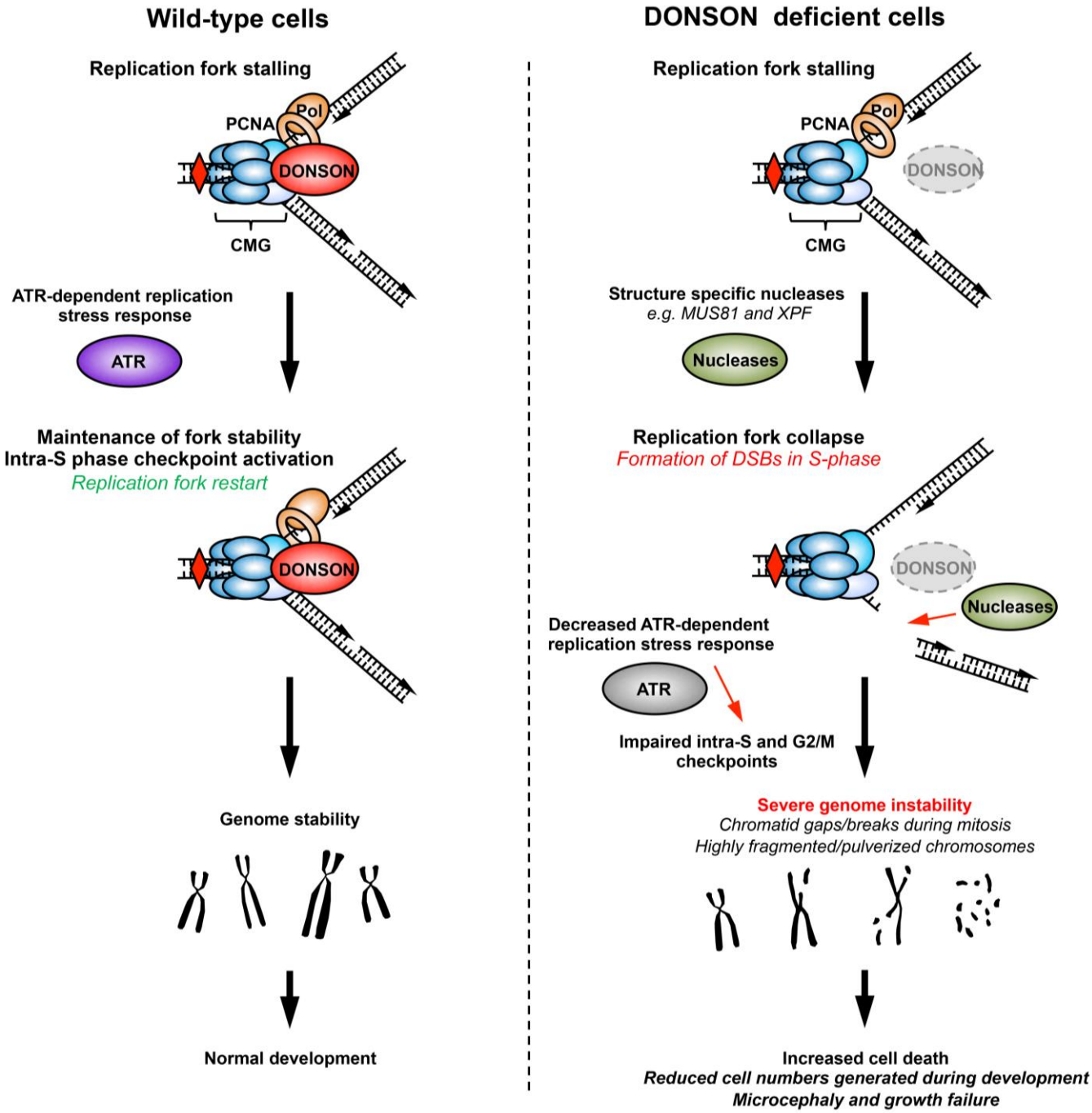

Supplementary Figure 22: Model depicting how DONSON mutations may lead to genome instability and microcephaly

DONSON is a component of the replisome, a very large macromolecular complex of over two hundred proteins, including key replication machinery, the CMG complex (CDC45, MCM2-7 and GINS), PCNA, and the replicative polymerases (Pol). **(a)** Upon replication stress (red diamond) and replication fork stalling, the presence of functional DONSON ensures maintenance of fork stability. The ATR-dependent replication stress response also contributes to ensuring replication fork stability, and promotes activation of the intra-S and G2/M phase checkpoints, preventing transmission of DNA damage through to mitosis, and ensuring genome stability. **(b)** In the absence of functional DONSON, stalled replication forks are cleaved by structure-specific nucleases, such as MUS81 and XPF, leading to the generation of DSBs in S-phase. Impaired S-phase and G2/M checkpoint function in the absence of DONSON facilitates the transit of DNA damage into subsequent phases of the cell cycle, resulting in elevated mitotic chromosome breaks that will increase cell death. In patients with mutations in DONSON, such increased cell death would lead to reduced numbers of cells being generated during development, resulting in the microcephaly and growth failure observed.

Supplementary Note:

Fluorescence Cross-Correlation Spectroscopy (FCCS)

Fluorescence imaging and Fluorescence Correlation Spectroscopy (FCS) measurements were performed on a uniquely modified confocal laser scanning microscopy system, the ConfoCor3 (Carl Zeiss, Jena, Germany), consisting of the Zeiss LSM780 inverted setup and comprising Diode 405 nm, Ar multiline 458, 488 and 514 nm, DPSS 561 nm and HeNe 633 nm lasers. It enables detection using silicon Avalanche Photo Detectors (APDs) (SPCM-AQR-1X; PerkinElmer, USA) for imaging and FCS. Images were recorded at a 1024X1024 pixel resolution. The C-Apochromat 40x/1.2 W UV-VIS-IR objective was used throughout. Fluorescence intensity fluctuations were recorded in arrays of 10 consecutive measurements, each measurement lasting 10 s. Averaged curves were analyzed using the ZEN software for online data analysis or exported and fitted offline. In either case, the nonlinear least square fitting of the autocorrelation curve was performed using the Levenberg–Marquardt algorithm. Quality of the fitting was evaluated by visual inspection and by residuals analysis. Control FCS measurements to assess the detection volume were routinely performed prior to data acquisition, using dilute solutions ($10\,nM$) of Alexa488 and CF^{TM}568 dyes. Highly purified double-stranded DNA, in which each strand carries one fluorophore of Alexa488 and Atto565, was used as a cross-correlation standard. 85% cross-correlation was measured using the FCCS standard, whereas 13% cross-correlation (due to cross-talk) was measured with the two dyes in solution (data not shown). The variation between independent measurements reflects variations between cells, rather than imprecision of FCS measurements.

FCS/FCCS measurements of GFP-DONSON/RFP-PCNA and GFP/RFP-PCNA expressing cells

HeLa cells stably expressing GFP-DONSON and mCherry-PCNA (construct kindly provided by C. Lukas, Copenhagen; referred to as RFP-PCNA) were grown under standard conditions overnight on chambered coverslips (µ-slide, 8 well, Ibidi) and the growth medium was replaced by L-15 medium (Leibovitz) (Sigma) immediately prior to FCS/FCCS measurements. Cells expressing low levels of RFP-PCNA/GFP-DONSON or RFP-PCNA/GFP were used for FCS/FCCS measurements. Measurements were made in weakly expressing cells only. As the concentration of RFP-PCNA in replication foci was observed to be several-fold higher than that of DONSON-GFP and GFP, only cells with similar GFP/RFP ratios were used for cross-correlation analysis and comparable GFP-DONSON and GFP only concentrations used for comparison.

Background on Fluorescence Microscopy Imaging and FCS

As described above, an individually modified instrument (Zeiss, LSM780, ConfoCor 3) with fully integrated FCS/CLSM optical pathways was used for imaging. The detection efficiency of CLSM imaging was significantly improved by the introduction of APDs. As compared to PMTs, which are normally used as detectors in conventional CLSM, the APDs are characterized by higher quantum yield and collection efficiency – about 70 % in APDs as compared to 15 – 25 % in PMTs, higher gain, negligible dark current and better efficiency

in the red part of the spectrum. Enhanced fluorescence detection efficiency enabled image collection using fast scanning ($1-5\ \mu s/pixel$). This enhances further the signal-to-noise-ratio by avoiding fluorescence loss due to triplet state formation, enabling fluorescence imaging with single-molecule sensitivity. In addition, low laser intensities ($150–750\ \mu W$) could be applied for imaging, significantly reducing the photo-toxicity.

FCS/FCCS measurements are performed by recording fluorescence intensity fluctuations in a very small observation volume element (OVE) of a prolate ellipsoid shape (about $500\ nm$ wide and about $1-1.5\ \mu m$ long) that is placed in GFP-DONSON/RFP-PCNA or control GFP/RFP-PCNA HeLa cells by focusing the laser light through the microscope objective and by collecting the fluorescence light through the same objective using a pinhole in front of the detector to block out-of-focus light. We established that observed fluorescence intensity fluctuations are caused by fluorescently labeled GFP-DONSON or RFP-PCNA molecules passing through the OVE and that the characteristic decay times of the autocorrelation functions do not depend on the concentration of GFP-DONSON or RFP-PCNA (**Supplementary Fig. 13**). Therefore, we analyzed the diffusion of the two proteins in the nucleus, using temporal autocorrelation analysis.

In temporal autocorrelation analysis we first derive the autocorrelation function G(τ):

$$G(\tau) = 1 + \frac{\langle \delta I(t) \cdot \delta I(t+\tau) \rangle}{\langle I(t) \rangle^2},$$

where $\delta I(t) = I(t) - \langle I(t) \rangle$ is the deviation from the mean intensity at time t and $\delta I(t + \tau) = I(t + \tau) - \langle I(t) \rangle$ is the deviation from the mean intensity at time $t + \tau$. For further analysis, an autocorrelation curve (ACC) is derived by plotting $G(\tau)$ as a function of the lag time, i.e. the autocorrelation time τ.

To derive information about molecular numbers and their corresponding diffusion time, the experimentally obtained ACCs are compared to autocorrelation functions derived for different model systems. A model describing free three-dimensional diffusion of two components was used for fitting Cross-Correlation Curves (CCCs) in this study, whereas a two-component model with triplet correction was used for fitting ACCs:

$$G(\tau) = 1 + \frac{1}{N}\left(\frac{1-y}{\left(1+\frac{\tau}{\tau_{D_1}}\right)\cdot\sqrt{1+\frac{w_{xy}^2\tau}{w_z^2\tau_{D_1}}}} + \frac{y}{\left(1+\frac{\tau}{\tau_{D_2}}\right)\cdot\sqrt{1+\frac{w_{xy}^2\tau}{w_z^2\tau_{D_2}}}}\right)\cdot\left(1+\frac{T}{1-T}\cdot e^{-\frac{\tau}{\tau_T}}\right)$$

In the above equation, *N* is the average number of molecules in the OVE; *y* is the fraction of the slowly moving GFP-DONSON and RFP-PCNA molecules; τ_{D_1} is the diffusion time of the free GFP-DONSON and RFP-PCNA molecules; τ_{D_2} is the diffusion time of GFP-DONSON and RFP-PCNA molecules undergoing interactions; w_{xy} and w_z are radial and axial parameters, respectively, related to spatial properties of the OVE; T is the average equilibrium fraction of molecules in the triplet state; and τ_T the triplet correlation time related to rate constants for intersystem crossing and the triplet decay. Spatial properties of the detection volume, represented by the square of the ratio of the axial and radial parameters ($\left(\frac{w_z}{w_{xy}}\right)^2$), are determined

in calibration measurements performed using a $10\,nM$ solution of Alexa488 and CF^{TM}568 for which the diffusion coefficient (D) is known. The diffusion time, τ_D, measured by FCS, is related to the translation diffusion coefficient *D* by:

$$\tau_D = \frac{w_{xy}^2}{4D}.$$